Atomic-scale structure of ZrO2 : Formation of metastable polymorphs

Alexandre Solomon, Eric O'quinn, Juejing Liu, Igor Gussev, Xiaofeng Guo, Joerg Neuefeind, Christina Trautmann, Rodney Ewing, Gianguido Baldinozzi, Maik Lang

Science Advances
AAAS

Article Content for

Atomic-Scale Structure of ZrO_2: Formation of Metastable Polymorphs

Alexandre P. Solomon *et al.*

*Corresponding author. Email: mlang2@utk.edu

FRONT MATTER

Title

- Atomic-Scale Structure of ZrO_2: Formation of Metastable Polymorphs
- Insight into Structure of Metastable ZrO_2

Authors

Alexandre P. Solomon,[1] Eric C. O'Quinn,[1] Juejing Liu,[2] Igor M. Gussev,[1,3] Xiaofeng Guo,[2] Joerg Neuefeind,[4] Christina Trautmann,[5] Rodney C. Ewing,[6] Gianguido Baldinozzi,[3] and Maik K. Lang[1,*]

Affiliations

[1] Department of Nuclear Engineering, University of Tennessee, Knoxville, TN, 37996, USA.

[2] Department of Chemistry, Washington State University, Pullman, WA, 99164, USA.

[3] SPMS, CNRS CentraleSupélec, Université Paris-Saclay, 91190 Gif-sur-Yvette, France.

[4] Spallation Neutron Source, Oak Ridge National Laboratory, Oak Ridge, TN, 37830, USA.

[5] GSI Helmholtzzentrum für Schwerionenforschung, 64291 Darmstadt, Germany.

[6] Department of Earth & Planetary Sciences, Stanford University, Stanford, California 94305, USA.

* Author to whom correspondence should be addressed. Electronic mail: mlang2@utk.edu.

Abstract

Metastable phases can exist within local minima in the potential energy landscape when they are kinetically "trapped" by various processing routes, such as thermal treatment, grain size reduction, chemical doping, interfacial stress, or irradiation. Despite the importance of metastable materials for many technological applications, little is known about the underlying structural mechanisms of the stabilization process and atomic-scale nature of the resulting defective metastable phase. Investigating ion-irradiated and nanocrystalline zirconia with neutron total scattering experiments, we show that metastable tetragonal ZrO_2 consists of an underlying structure of ferroelastic, orthorhombic nanoscale domains stabilized by a network of domain walls. The apparent long-range tetragonal structure that can be recovered to ambient conditions is only the configurational ensemble average of the underlying orthorhombic domains. This structural heterogeneity with a distinct short-range order is more broadly applicable to other non-equilibrium materials and provides insight into the synthesis and recovery of functional metastable phases with unique physical and chemical properties.

Teaser

Experimentation confirms an orthorhombic metastable ZrO_2 phase, yielding insight into metastable phase synthesis and recovery.

MAIN TEXT

Introduction

Materials selection for engineering applications generally relies on an equilibrium phase diagram that describes thermodynamic stability with respect to chemical composition, as well as temperature and pressure. Metastable polymorphs can be stabilized by slow kinetic pathways to a stable phase, thus expanding the number of accessible phases beyond their usual phase space (*1, 2*). Stabilization beyond equilibrium phase space is especially useful because metastable phases often have superior material properties attractive for a myriad of technological applications (*3*). Exceptional mechanical strength (*4*), fast ionic and high/low thermal conduction (*5, 6*), and enhanced electrical/optical properties (*7*) arise in metastable compounds when synthesis and processing yield their stabilization at expected operating conditions.

From an engineering point of view, induced strain is a common strategy in the stabilization process, as defects and surfaces modify the free energy landscape and affect phase stability (*8*). Strain for the purpose of metastable phase synthesis can be introduced by various means, such as reduction to nanoscale size (*9*), growth on a template/substrate (*10, 11*), thermal/pressure quenching (*12*), mechanical processing (*1, 13*), doping (*14*), and irradiation (*15*). Structural aspects of metastability, particularly defect-engineered stabilization mechanisms, must be better understood at the atomic scale in order to develop novel synthesis routes and accelerate the discovery of new metastable phases desirable for next-generation technologies.

Metastability plays a particularly important role in well-studied zirconia (ZrO_2), which exhibits structural transformations among several polymorphs that occur under a wide range of temperature and pressure conditions (*16, 17*). At standard pressure and temperature, the stable atomic configuration is the monoclinic ($P2_1/c$) phase, commonly known as baddeleyite, where the number of oxygen neighbors coordinated with each zirconium atom is 7 (Fig. S1). Two distinct structures, the high-temperature tetragonal ($P4_2/nmc$) and cubic ($Fm\text{-}3m$, isostructural with fluorite) polymorphs, both with a Zr coordination number of 8, can be obtained upon heating above approximately 1400 K and 2600 K, respectively (*18, 19*). Two additional orthorhombic polymorphs with coordination numbers of 7 (*Pbca*) and 9 (*Pnam*) are accessible at high pressure (*16*), and a polar orthorhombic phase ($Pca2_1$) accounts for ferroelectricity in ZrO_2 thin films (*20*). The tetragonal and monoclinic structures of ZrO_2 are related by a displacive phase transformation mechanism involving structural distortions and shear deformations (*21*).

Tetragonal zirconia-based ceramics, like the cubic high-temperature polymorph, are a remarkably useful material for many technologies, owing to impressive mechanical (high strength and toughness), thermal (refractory with low conductivity), and electrical (high dielectric permittivity with fast oxygen conductivity when doped) properties (*14*). However, tetragonal ZrO_2 is not stable at ambient conditions, and the reversible phase

transformation yields the monoclinic phase upon cooling (*22*). Since tetragonal zirconia cannot be thermally quenched in bulk form, stabilization is typically achieved by aliovalent doping of ZrO_2 (i.e., $Y_xZr_{1-x}O_{2-0.5x}$ – partially stabilized zirconia), thereby introducing anion vacancies, substitutional defects, and changes in stoichiometry (*18*). While stabilization *via* doping changes the chemical composition, the tetragonal phase can also be produced in pure stoichiometric ZrO_2 when prepared as a nanocrystalline material, either as a nanometric layer on a substrate (*10, 11*) or as a nanocrystalline powder (*23*). The stabilization mechanism at the nanoscale was described by Garvie *et al.* (*23*) more than 50 years ago as being driven by strain energy originating from surfaces or interfaces when the characteristic length scale of the system is smaller than ~30 nm (*14*).

Ion irradiation, which has also been demonstrated to quench metastable high-temperature and high-pressure phases to ambient conditions in numerous cases (*15, 24*), can similarly be utilized to transform monoclinic ZrO_2 to the tetragonal polymorph (*25*). In this case, radiation-induced defects and associated strain fields are believed to be responsible for stabilization, regardless of whether these defects are produced by displacive, knock-on collisions (neutron or low-energy MeV ion irradiation) (*8*) or by extreme electronic excitations and ionization processes (high-energy GeV ion irradiation) (*16*). The long-range order of each crystalline polymorph, and in particular the monoclinic-to-tetragonal transformation as a function of temperature (*19*), ion irradiation (*26*), and crystallite size (*14*), has been thoroughly characterized using a wide range of analytical techniques, yet the atomic-scale processes involved in the stabilization of metastable phases are not fully understood. Therefore, zirconia serves as an apt model system to unravel the interplay between structural complexity and phase metastability.

Results

Multi-Length Scale Characterization

Neutron total scattering, with high sensitivity to the oxygen sublattice, was performed at the world's most intense spallation source at Oak Ridge National Laboratory and used to simultaneously probe the short-range order (SRO) and long-range order (LRO) of the metastable tetragonal polymorph. For this study, the metastable phase was prepared by two approaches: as nanocrystalline ZrO_2 (grain size: ~7 nm) and from microcrystalline ZrO_2 processed by intense energetic heavy ion irradiation (1.47 GeV Au ions). Both the SRO and LRO were analyzed using small-box modeling in real-space and Rietveld refinement in reciprocal space. A multi-length scale simulation of a supercell consisting of several nanoscale domains provided additional insight into how the LRO emerges through averaging of SRO building blocks.

Room temperature neutron (Figs. S2, S3) and synchrotron X-ray diffraction (Fig. 1a) independently confirm that the LRO of the pristine, microcrystalline ZrO_2 sample is the well-known monoclinic polymorph. As expected, the LRO in both nanocrystalline and ion-irradiated microcrystalline ZrO_2 is best described by a structural model derived from the high-temperature tetragonal polymorph (Fig. 1a) (*14, 17*). The X-ray diffraction (XRD) pattern of the ion-irradiated sample contains minor (<5%) monoclinic contributions remaining from regions of unirradiated material with incomplete ion-track overlap. The

nanocrystalline ZrO_2 is completely phase-pure, and the pronounced peak broadening is characteristic of the small crystallite size (*27*) without any detectable splitting of the tetragonal peaks or emergence of additional peaks. No oxygen vacancies were detected by Rietveld analyses or indicated by a change in color of the sample.

The SRO was examined in the three samples by analyzing the high-resolution neutron pair distribution functions (PDFs). This real-space structural representation is a histogram of interatomic distances that quantifies the probability that two atoms are separated by a distance, *r* (*28*) (Fig. 1b). The PDF was initially modeled for all three samples using the atomic positions derived from refinement of the X-ray diffraction patterns (Fig. 1a), i.e., the LRO. As demonstrated by the difference curve, the monoclinic model accurately fits the PDF of the unirradiated, microcrystalline reference sample, indicating a uniform organization across all spatial length scales (i.e., structural homogeneity). In contrast, a significant deviation from the long-range symmetry is observed in the non-equilibrium phases. The tetragonal structural model (*29*) fails to describe the PDFs of both metastable zirconia samples at $r < 7$ Å, representing a volume consisting of about three tetragonal unit cells; the mismatch becomes increasingly pronounced for interatomic distances shorter than ~4 Å. On the other hand, the accuracy of the tetragonal model improves at longer distances (Fig. 1b), indicating a structural discontinuity and spatial heterogeneity with the LRO not accurately describing the underlying atomic-scale configuration. This agrees with prior X-ray PDF of thin-film zirconia, where reduced local symmetry associated with oxygen vacancies explained the short-range deviation from tetragonal symmetry in substoichiometric ZrO_{2-x} (*10*). However, regardless of whether the metastable tetragonal phase was obtained as a nanomaterial or by ion irradiation, no deviation from stoichiometry was detected by neutron PDF analysis.

Even more remarkably, none of the conventional ambient (monoclinic $P2_1/c$, 14), high-temperature (tetragonal $P4_2/nmc$, 137; cubic *Fm-3m*, 225) (*19*), or high-pressure phases (ortho-I *Pbca*, 61; ortho-II *Pnma*, 62) (*16*) reported in the equilibrium phase diagram, or their combinations, describe the short range order (Fig. S4). Deviations from the tetragonal model in nanocrystalline ZrO_2 have been hinted at previously in X-ray PDF and Extended X-ray Absorption Fine Structure (EXAFS) studies of nanopowders and in thin-films, where they were explained as lower symmetry distortions of coordination polyhedra or as "shear-jamming" of their packing sequences (*9, 10, 30*). However, the analytical methods employed in previous investigations lack either the direct real-space resolution or the high oxygen sensitivity characteristic of the neutron PDF analysis.

Landau Theory

To gain further insight into the local structure of metastable zirconia, representation theory (*31*) was employed to describe the transformation pathway between the high-temperature tetragonal and the ambient monoclinic phases. The Landau energy landscape associated with this transformation, qualitatively shown in Figure 2a, is characterized by two structural instabilities which can be described by a sequence of two phonon condensations (*32*) (see also Supplementary text). Cooling a tetragonal bulk ZrO_2 crystal triggers the condensation of a first phonon (M1), yielding an unstable orthorhombic *Pbcn* structure,

immediately followed by the condensation of a second phonon (M3), rendering the monoclinic ground state phase.

Thus, the tetragonal and monoclinic phases are structurally linked by an intermediate orthorhombic *Pbcn* phase, occurring at a saddle point of the Landau energy landscape (*32*). Despite many efforts, this predicted orthorhombic phase has never been observed experimentally, as it is unstable in the unirradiated bulk ZrO_2 system (*19*); however, the *Pbcn* structural model accurately describes the bonding environment and atomic configuration of the two metastable ZrO_2 samples, as demonstrated by the small-box refinement of neutron PDF data for *r*-values up to 6 Å (Fig. 3a). Refined structural parameters are given in Table S1 and can be used to construct the orthorhombic phase observed here. In contrast with the high-pressure orthorhombic and ambient monoclinic phases, the Zr cation maintains a statically distorted eight-fold coordination with the O anions in the *Pbcn* structure, but the distribution of bond lengths is broader than that permitted by the tetragonal model.

To further probe the existence of the orthorhombic atomic arrangement within metastable ZrO_2, the nanocrystalline sample was additionally analyzed using synchrotron-based EXAFS (*33*) (Fig. 3b and Table S2). The PDF-derived *Pbcn* and $P4_2/nmc$ (*29*) structural models were used with fixed coordination numbers for a better comparison. When applying the *Pbcn* model to the EXAFS data, a higher level of accuracy was achieved, yielding lower residuals ($R_w = 0.034$) and more physically meaningful parameters (Table S2). In contrast, the $P4_2/nmc$ structure does not accurately fit the data, resulting in a much higher residual ($R_w = 0.169$), particularly evident in the Zr–Zr scattering paths between 2.8 and 4.0 Å (Fig. 3b). Thus, the EXAFS analysis independently confirms the existence of an orthorhombic SRO in tetragonal ZrO_2 nanopowders, explaining deviations previously reported in EXAFS data of metastable zirconia (*9, 30*).

Supercell Modeling

The local atomic configuration of metastable zirconia is fully described by the orthorhombic structural model in the neutron PDF data (Fig. 3a). Since there are no short-range contributions in the PDF from the tetragonal phase, this is clear evidence that there is no coexistence of both phases in the material. The formation of the orthorhombic atomic arrangement is the consequence of the improper ferroelastic phase transition (*32*) driven by an instability at the tetragonal Brillouin zone boundary M point (for more information see Supplementary Materials). Disrupting the transition illustrated in Figure 2a after the condensation of the first phonon produces degenerate, ferroelastic, orthorhombic domains, differing only by their lattice orientation and origin shift. Correlated atomic displacements related to the *Pbcn* symmetry are maintained only within a single domain. Box-car refinements of neutron PDFs reveal that the correlation length of each orthorhombic domain is approximately 2 nm (Fig. S5), consistent with the absence of orthorhombic Bragg peaks in the high-resolution XRD data displayed in Figure 1a and the neutron diffraction data shown in Figure S2. Thus, the apparent tetragonal phase must be the result of an ensemble average of these orthorhombic nanodomains. Group-subgroup symmetry analysis between the *Pbcn* (SRO) and $P4_2/nmc$ (LRO) space groups indicates that four orientational domain variants are required to establish the tetragonal structure (*34*). Figure

4 illustrates the unique combination of symmetry operations, superlattice basis, and specific origin choice that produces each variant (see Supplementary text for detailed derivation). These individual *Pbcn* variants are spatially distinguished and separated by a nanoscale network of domain walls (*35, 36*).

This structural complexity and heterogeneous behavior cannot be fully captured by small-box modeling, which assumes homogeneity across all length-scales. Additionally, PDF refinement does not provide insight into the structural transition from orthorhombic SRO correlations to tetragonal LRO correlations. Therefore, a new structural model shown in Figure 5a was created based on all four orientational variants (Fig. 4) of the 2-nm sized orthorhombic domains, assembling a 4 × 4 × 0.5 nm supercell, totaling 768 atoms. Atomic positions were restricted in each domain according to *Pbcn* symmetry, and each domain was separated by domain walls and distinguished by its relative orientation (tilted text in Fig. 5a) and phase shift (gray text in Fig. 5a). Each domain within the supercell retained the structural parameters and symmetry constraints of the original *Pbcn* refinement with respect to its own internal origin, but in each case rotated or phase shifted with respect to one another. In this supercell, pair correlations describing distances between atoms within each individual orthorhombic domain are identical to each other, even when the domain orientations are different. On the other hand, pair correlations describing distances between atoms across domain walls produce an apparent tetragonal symmetry; circled atoms in Figure 5a highlight several intra- and inter-domain pair correlations.

The XRD pattern of the refined supercell (Fig. 5b) was simulated with GSAS-II (*37*) and reproduces a subset of peaks with narrow widths that can be fully indexed as tetragonal (with $\mathbf{a}_O \approx \mathbf{c}_O$). Comparison to the experimental data (Fig. 5b) shows that the tetragonal LRO can be entirely reproduced by this ensemble average of orthorhombic nanodomains (*38*).

A neutron PDF was further simulated for the supercell, refined using PDFgui, and compared to the experimental data (Fig. 5c). The simulated PDF accurately captures the structural transition from orthorhombic correlations to long-range tetragonal correlations. Both the orthorhombic model and supercell model capture the short-range correlations equally well when refined over the same length scale (up to ~10 Å). This supercell analysis independently confirms the hypothesis that non-equilibrium zirconia consists of nanoscale orthorhombic domains, separated by domain walls, which yield the tetragonal long-range structure by ensemble averaging. This is in clear contrast with the equilibrium picture of a tetragonal high-temperature phase that is homogeneous across all structural length scales. The supercell quality of the fit to the PDF could be further improved by enlarging the supercell to capture all possible orientational relations between individual orthorhombic domains; due to limitations of building the supercell manually we considered only one possible configuration.

Stabilization Mechanism

This insight into the structural behavior of metastable zirconia with the existence of an otherwise transient orthorhombic atomic arrangement bears important information on its stabilization mechanism. Recovery of orthorhombic domains implies that the condensation of the second phonon (M3) is suppressed, requiring an energy barrier that converts the saddle-point into a local minimum in the energetic landscape (Fig. 2b). Details of the

underlying structural processes remain speculative based on experimental data alone; however, an interplay of defects and domain walls must play a key role in the stabilization. Orthorhombic domains are an unstable, transient state in the tetragonal-to-monoclinic transformation under equilibrium conditions (*19, 32*). Under non-equilibrium conditions, characterized by high defect densities, domain walls are elastically pinned and become less mobile (*39, 40*). This forms a network of persistent domain walls, which are a structural barrier that prevents the condensation of the second phonon (M3).

This intriguing process applies equally to both sample preparation techniques and defect formation mechanisms (nanocrystal synthesis and ion irradiation), suggesting that the interplay of domain walls and defects is a more general stabilization mechanism in zirconia. These defects can be destabilized by thermal annealing, allowing coarsening of the orthorhombic nanodomains and recovery of the monoclinic polymorph observed during heating (*41*). The expression of a distinct, ordered atomic arrangement within highly defective zirconia agrees also with previous research on disordered ceramics that rationalized the existence of short-range order and structural heterogeneity by a straightforward application of Pauling's rules (*42*). The orthorhombic domain structure, and in particular the network of domain walls, may be an efficient way of accommodating high levels of structural defects by minimizing the impact on the overall structure.

Discussion

The most important question that remains is whether the structures of other metastable phases are also inherently heterogeneous with short-range order not described by the equilibrium phase diagram. As summarized in Figure 6, many material systems obtained by far-from-equilibrium processing show a long-range structure that consists of an underlying network of nanodomains with distinct, unexpected symmetry (*43, 44*). Pyrochlore oxides irradiated by high-energy ions or processed by intense mechanical action illustrate this effect (*45, 46*). For example, ball-milled $Yb_2Sn_2O_7$ consists of nanodomains with an orthorhombic weberite-type structure (Fig. S6). As for non-equilibrium zirconia, these domains yield a metastable high symmetry structure across the long-range through configurational averaging (in this case, a cubic defect fluorite structure). A weberite-type atomic arrangement is not represented in the phase diagram of $A_2B_2O_7$ pyrochlore-type oxides and cannot be synthesized as a stable long-range structure (*47*); however, as with zirconia, it is the preferred atomic arrangement within the metastable phase.

This structural theme can be further expanded to other synthesis and processing methods (*e.g.*, doping and substrate growth) which produce materials that occupy neither the ground state, nor the stable high-temperature/pressure phase observed over macroscopic length scales (Fig. 6). Instead, these metastable materials consist of an assembly of nanoscale domains with a distinct local atomic arrangement that is, like orthorhombic zirconia, trapped within a local minimum of the free energy landscape (Fig. 2b). This improved structural description also applies to out-of-equilibrium materials used in many technological applications (*6, 48*). For example, yttria-stabilized cubic zirconia exhibits high strength and toughness and is used in many everyday technologies such as grinding and cutting tools (*14, 18*). In this case, doping leads to the recovery of the desired cubic high-temperature phase. Our data (not shown here) along with previous studies (*49, 50*) reveal that this material phase consists of local nano-scale domains of lower symmetry.

Thin-film (*10*) and template-grown materials used as multiferroics in numerous devices, including field-effect transistors (FETs) and high-density ferroram (FeRAM) memory (*51-53*) are inherently metastable. These systems have potential uses in exceptionally fast and dense next-generation nonvolatile memory and other microelectronics, enabling further minimization of electronic component size and reduced power consumption (*54, 55*). Their functional properties and performance critically depend on nanoscale engineering of interfaces and lower symmetry nanodomains that can average to an apparent higher symmetry structure.

Finally, we suggest that predicting the metastable phases that manifest at the sub-nanometer scale is possible when displacive transformations involve the condensation of multiple phonons (*19, 32*). Analyzing the structural distortion modes of parent space-group symmetry with the ISODISTORT software (*56*) identifies displacive pathways between crystalline structures and accurately suggests the *Pbcn* structure as an intermediate phase in the tetragonal-to-monoclinic phase transition of ZrO_2.

Using tetragonal ZrO_2 and neutron total scattering, we have provided an important aspect of metastable phases with respect to their atomic-scale structure and stabilization mechanism. We revealed that the recovered metastable phase is structurally highly heterogeneous, and the short-range order is best described by an orthorhombic (*Pbcn*) atomic configuration, presenting the first experimental validation of this previously predicted structural zirconia polymorph. During the two-step displacive tetragonal-to-monoclinic phase transformation, this orthorhombic phase is unstable and exists only as a highly transient structural state in pristine, bulk ZrO_2 (*19*). However, under non-equilibrium conditions and high defect concentrations, these nanoscale orthorhombic domains are recovered and stabilized by immobilization of domain walls. The interplay of domain walls and defects forms structural barriers which prevent shear of atomic planes and condensation of the M3 phonon. Orthorhombic nanoscale domains are stabilized to ambient conditions by a modified energetic landscape and yield an apparent tetragonal phase by configurational averaging.

We have shown here that an inherent structural heterogeneity with a distinct short-range order is more broadly applicable to other metastable ceramics that are synthesized or processed under non-equilibrium conditions. If a similar stabilization concept characterized by an interplay of nanodomain walls and defects applies also to metastable materials prepared under high pressure, this may offer a pathway to recover currently unquenchable high-pressure phases (*48*), which still presents one of the greatest challenges in high-pressure science (*3*). This is of great interest since many of these material phases exhibit unusual and useful properties, such as near-room temperature superconductivity (*57*), ultrahigh density hydrogen storage capabilities (*58*), and superior hardness (*48*). In fact, the concept of structural competition across length scales is already utilized in the development and optimization of functional metastable thin films. An example is HfO_2, in which nanoscale metastable polar phases exhibit ferroelectric properties that are suppressed when domains interconnect beyond a critical thickness or after repeated cycling (*51*). By coupling advanced short-range characterization methods with sufficiently high sensitivity and resolution, such as neutron PDF analysis, with representation theory, investigations of other metastable materials can further expand on the proposed phase

stabilization concept. Extensive modeling is then required to apply these findings in the discovery of novel metastable phases with useful properties.

Materials and Methods

Sample Preparation

Pure (99.7%) microcrystalline "bulk" ZrO_2 was purchased from Alfa Aesar, and the concentrations of impurity cations which could stabilize the tetragonal phase (Ca, Y, Ce, Mg, Ti) were verified to be less than 100 ppm using a CAMECA SX100 electron microprobe. A nanocrystalline ZrO_2 sample was prepared by the decomposition of anhydrous zirconyl chloride by dissolving a $ZrCl_4$ precursor in deionized water to form a 0.025 M solution, which was sprayed into liquid nitrogen, forming frozen droplets with diameters on the order of micrometers. The frozen solution was dried at 0.04 mbar using a Christ Alpha 2–4 LSC freeze drier, resulting in anhydrous zirconyl chloride ($ZrOCl_2$) powder. The dry samples were heated at 450˚C for 15 minutes to eliminate the chloride and produce pure ZrO_2 while limiting grain growth. XRD patterns acquired on a PANalytical X'Pert PRO diffractometer were analyzed using Rietveld refinement (*59*), confirming that the nanoparticles crystallized in the tetragonal phase and quantifying the nanocrystallite diameter (7.2 ± 0.2 nm – small enough to prevent any texture effects from anisotropic growth of crystallites).

Sample Irradiation

To stabilize the metastable tetragonal phase of stoichiometric ZrO_2, pure (99.7%) bulk ZrO_2 from Alfa Aesar was irradiated in vacuum with 1.47 GeV Au ions to a fluence of 10^{13} ions/cm^2 using the X0 beamline of the UNILAC heavy ion accelerator at the GSI Helmholtz Centre for Heavy Ion Research. Samples were placed in cylindrical aluminum chambers with 1 cm diameter. The sample thickness was chosen using the SRIM-2013 software package (*60*) to calculate the limited penetration depth (27 μm) over which the ions deposit a constant energy per track length ($dE/dx = 40 \pm 2$ keV/nm), ensuring complete ion penetration and homogeneous energy deposition throughout the sample volume. These irradiation conditions are tailored to produce quantities of fully irradiated material on the order of 100 mg, specifically enabling characterization by neutron total scattering in addition to conventional X-ray characterization techniques. More information about this irradiation scheme can be found elsewhere (*43, 45, 61*).

Data Acquisition and Analysis

Synchrotron X-ray diffraction (SXRD) experiments were performed at Brookhaven National Laboratory using the PDF (28-ID-1) beamline of the National Synchrotron Light Source-II (NSLS-II) (*62*). High-resolution XRD patterns were measured at room temperature with 60 second exposure times for each of the pristine bulk, nanocrystalline, and irradiated powders loaded in 0.0395" (inner diameter) Kapton tubes with wall thickness of 0.0020" using an X-ray energy of 74.474 keV ($\lambda = 0.1665$ Å) while scanning the beam along the length of the sample to ensure good powder averaging. An identical empty Kapton tube was measured for proper background subtraction, and a LaB6 660b

NIST standard was measured to calibrate the detector and produce the instrument parameter file for subsequent Rietveld analysis.

Neutron total scattering was performed using the time-of-flight neutron diffraction NOMAD instrument (*63*) (BL-1B) of the Spallation Neutron Source at Oak Ridge National Laboratory. Samples were poured into 2 mm quartz capillaries with wall thickness of 0.01 mm and, to standardize neutron exposure among measurements, placed in the neutron beam until the protons incident on the liquid mercury target reached a total charge of 8 coulombs (around 90 minutes) at 300 K. Additional measurements were performed using a diamond powder standard to ensure proper detector pixel calibration, and an identical empty quartz capillary was measured for proper background subtraction. Additional low-temperature measurements were performed at 100 K for the bulk and irradiated samples to minimize the effect of thermal vibrations. The scattering from the empty capillary was subtracted from the scattering collected from the sample, and the resulting scattering function, $S(Q)$, was normalized to the scattering from a vanadium rod. The experimental pair distribution functions (PDFs) were produced by the Fourier transform of $S(Q)$ using the following equation:

$$G(r) = \frac{2}{\pi}\int_{Q_{min}}^{Q_{max}} Q[S(Q) - 1]\sin(Qr)\,dQ \qquad (1),$$

with a maximum momentum transfer, Q, of 31.4 $Å^{-1}$ for the irradiated sample and 30.0 $Å^{-1}$ for the nanocrystalline sample. No Lorch functions or other smoothing functions were applied to any of the total scattering data.

The diffraction data were analyzed using the Rietveld refinement method (*59*), which was performed for each of the X-ray and neutron diffraction patterns with the GSAS-II software package (*37*). Refinements were performed for the nanocrystalline sample using 13 parameters: scale, unit cell parameters (a and c), atomic positions, isotropic atomic displacement parameters, microstrain, and six background coefficients. Refinements were performed for the irradiated sample in the same way, with one additional scale factor corresponding to the phase fraction of the remaining monoclinic phase. The monoclinic structure was refined from diffraction patterns of bulk, unirradiated sample using 26 parameters: scale, phase fraction, unit cell parameters (a, b, c, β), atomic positions, isotropic atomic displacement parameters, microstrain, grain size, and six background coefficients. All neutron diffraction pattern refinements were performed using data collected by detector banks 3, 4, and 5 of NOMAD (refining each data set separately).

Pair distribution function analysis of both the nanocrystalline and irradiated samples was conducted using the PDFgui small-box refinement software (*64*). The 16 refined parameters included the scale, unit cell parameters ($a \neq b \neq c$ for orthorhombic cells and $a = b \neq c$ for tetragonal cells), atomic positions, anisotropic atomic displacement parameters, nanocrystallite size, and a variable parameter, "delta2", to account for correlated atomic motion. Attempts were made to fit the high-temperature and high-pressure phases to the experimental PDFs of both samples (Fig. S4). Experimental PDFs of irradiated and nanocrystalline ZrO_2 were successfully fit using orthorhombic (*Pbcn*) symmetry for the short-range (r < 1 nm) and tetragonal ($P4_2/nmc$) symmetry for the long-range (r > 1 nm). In the region between, experimental PDFs were additionally fit as a two-phase system with

isotropic atomic displacement parameters using the boxcar method to determine whether a two-phase mixture was physically present (Fig. S5).

X-ray Absorption experiments were performed at beamline 16-BM-D of the Advanced Photon Source (APS) using the molybdenum sample holder configuration described by Lang *et al*. (*65*). A Zr metal foil was used as a calibrant, and the K-edge of Zr was probed by Extended X-ray Absorption Fine-Structure (EXAFS) analysis. EXAFS spectra of bulk, irradiated, and nanocrystalline ZrO_2 were all measured in transmission mode at room temperature. Using a Si(111) double-crystal monochromator, the X-ray energy was controlled between 17.600 and 19.000 keV with a variable step size ranging from 1 eV at the K-edge to 8 eV in the far post-edge region. The collection time at each energy step was 0.5 seconds, and each absorption scan was repeated 3 times. Background subtraction, post-edge removal, and Fourier transform were done using the Athena software package (*66*). The $P4_2/nmc$ and *Pbcn* structures refined from XRD patterns and neutron PDF, respectively, were used to fit the EXAFS spectra. EXAFS fits are presented in Figure 3b, and fit parameters are given in Table S2.

References

1. C. Suryanarayana, Mechanical alloying and milling. *Progress in Materials Science* **46**, 1-184 (2001).
2. D. B. Miracle, O. N. Senkov, A critical review of high entropy alloys and related concepts. *Acta Materialia* **122**, 448-511 (2017).
3. W. Mao, Y. Lin, Making the most of metastability. *Science* **377**, 814-815 (2022).
4. Z. M. Li, K. G. Pradeep, Y. Deng, D. Raabe, C. C. Tasan, Metastable high-entropy dual-phase alloys overcome the strength-ductility trade-off. *Nature* **534**, 227-+ (2016).
5. J. Lian, L. Wang, J. Chen, K. Sun, R. C. Ewing, J. M. Farmer, L. A. Boatner, The order-disorder transition in ion-irradiated pyrochlore. *Acta Materialia* **51**, 1493-1502 (2003).
6. A. A. Balandin, Thermal properties of graphene and nanostructured carbon materials. *Nature Materials* **10**, 569-581 (2011).
7. H. Tang, K. Prasad, R. Sanjines, P. E. Schmid, F. Levy, ELECTRICAL AND OPTICAL-PROPERTIES OF TIO2 ANATASE THIN-FILMS. *Journal of Applied Physics* **75**, 2042-2047 (1994).
8. D. Simeone, G. Baldinozzi, D. Gosset, S. LeCaer, L. Mazerolles, Impact of radiation defects on the structural stability of pure zirconia. *Physical Review B* **70**, (2004).
9. L. M. Acuna, D. G. Lamas, R. O. Fuentes, I. O. Fabregas, M. C. A. Fantini, A. F. Craievich, R. J. Prado, Local atomic structure in tetragonal pure ZrO2 nanopowders. *Journal of Applied Crystallography* **43**, 227-236 (2010).
10. N. Nakamura, L. S. Su, H. Wang, N. Bernstein, S. K. Jha, E. Culbertson, H. Y. Wang, S. J. L. Billinge, C. S. Hellberg, B. Reeja-Jayan, Linking far-from-equilibrium defect structures in ceramics to electromagnetic driving forces. *J. Mater. Chem. A* **9**, 8425-8434 (2021).
11. A. C. Dippel, M. Roelsgaard, U. Boettger, T. Schneller, O. Gutowski, U. Ruett, Local atomic structure of thin and ultrathin films via rapid high-energy X-ray total scattering at grazing incidence. *IUCrJ* **6**, 290-298 (2019).

12. T. Y. Xiao, Y. Nagaoka, X. R. Wang, T. Jiang, D. LaMontagne, Q. Zhang, C. Cao, X. Z. Diao, J. H. Qiu, Y. R. Lu, Z. W. Wang, Y. C. Cao, Nanocrystals with metastable high-pressure phases under ambient conditions. *Science* **377**, 870-874 (2022).
13. M. Gateshki, V. Petkov, G. Williams, S. K. Pradhan, Y. Ren, Atomic-scale structure of nanocrystalline ZrO2 prepared by high-energy ball milling. *Physical Review B* **71**, 9 (2005).
14. S. Shukla, S. Seal, Mechanisms of room temperature metastable tetragonal phase stabilisation in zirconia. *International Materials Reviews* **50**, 45-64 (2005).
15. A. P. Solomon, C. L. Tracy, E. C. O'Quinn, D. Severin, M. K. Lang, Transformations to amorphous and X-type phases in swift heavy ion-irradiated Ln(2)O(3) and Mn2O3. *Journal of Applied Physics* **129**, 10 (2021).
16. B. Schuster, F. Fujara, B. Merk, R. Neumann, T. Seidl, C. Trautmann, Response behavior of ZrO2 under swift heavy ion irradiation with and without external pressure. *Nuclear Instruments & Methods in Physics Research Section B-Beam Interactions with Materials and Atoms* **277**, 45-52 (2012).
17. G. Fadda, G. Zanzotto, L. Colombo, First-principles study of the effect of pressure on the five zirconia polymorphs. I. Structural, vibrational, and thermoelastic properties. *Physical Review B* **82**, 13 (2010).
18. J. Chevalier, L. Gremillard, A. V. Virkar, D. R. Clarke, The Tetragonal-Monoclinic Transformation in Zirconia: Lessons Learned and Future Trends. *Journal of the American Ceramic Society* **92**, 1901-1920 (2009).
19. D. Simeone, G. Baldinozzi, D. Gosset, M. Dutheil, A. Bulou, T. Hansen, Monoclinic to tetragonal semireconstructive phase transition of zirconia. *Physical Review B* **67**, 8 (2003).
20. J. Muller, T. S. Boscke, U. Schroder, S. Mueller, D. Brauhaus, U. Bottger, L. Frey, T. Mikolajick, Ferroelectricity in Simple Binary ZrO2 and HfO2. *Nano Lett.* **12**, 4318-4323 (2012).
21. J. W. Christian, G. B. Olson, M. Cohen, Classification of displacive transformations: What is a martensitic transformation? *J. Phys. IV* **5**, 3-10 (1995).
22. Y. Zhang, H. X. Chen, L. Duan, J. B. Fan, L. Ni, V. Ji, A comparison study of the structural and mechanical properties of cubic, tetragonal, monoclinic, and three orthorhombic phases of ZrO2. *Journal of Alloys and Compounds* **749**, 283-292 (2018).
23. R. C. Garvie, OCCURRENCE OF METASTABLE TETRAGONAL ZIRCONIA AS A CRYSTALLITE SIZE EFFECT. *J. Phys. Chem.* **69**, 1238-& (1965).
24. M. Lang, F. X. Zhang, J. M. Zhang, J. W. Wang, J. Lian, W. J. Weber, B. Schuster, C. Trautmann, R. Neumann, R. C. Ewing, Review of A(2)B(2)O(7) pyrochlore response to irradiation and pressure. *Nuclear Instruments & Methods in Physics Research Section B-Beam Interactions with Materials and Atoms* **268**, 2951-2959 (2010).
25. K. E. Sickafus, H. Matzke, T. Hartmann, K. Yasuda, J. A. Valdez, P. Chodak, M. Nastasi, R. A. Verrall, Radiation Damage Effects in Zirconia. *J. Nucl. Mater.* **274**, 66 (1999).
26. A. Benyagoub, Mechanism of the monoclinic-to-tetragonal phase transition induced in zirconia and hafnia by swift heavy ions. *Physical Review B* **72**, 094114 (2005).
27. G. K. Williamson, W. H. Hall, X-RAY LINE BROADENING FROM FILED ALUMINIUM AND WOLFRAM. *Acta Metallurgica* **1**, 22-31 (1953).

28. D. A. Keen, A. L. Goodwin, The crystallography of correlated disorder. *Nature* **521**, 303-309 (2015).
29. B. Bondars, G. Heidemane, J. Grabis, K. Laschke, H. Boysen, J. Schneider, F. Frey, Powder diffraction investigations of plasma sprayed zirconia. *J. Mater. Sci.* **30**, 1621-1625 (1995).
30. M. Dapiaggi, F. Maglia, L. Pagliari, I. G. Tredici, N. Rotiroti, The role of local structural distortions in the stabilisation of undoped nanocrystalline tetragonal zirconia. *Mater. Chem. Phys.* **147**, 395-402 (2014).
31. W. Cochran, CRYSTAL STABILITY AND THE THEORY OF FERROELECTRICITY. *Adv. Phys.* **9**, 387-423 (1960).
32. K. Negita, H. Takao, CONDENSATIONS OF PHONONS AT THE TETRAGONAL TO MONOCLINIC PHASE-TRANSITION IN ZRO2. *Journal of Physics and Chemistry of Solids* **50**, 325-331 (1989).
33. P. A. Lee, P. H. Citrin, P. Eisenberger, B. M. Kincaid, EXTENDED X-RAY ABSORPTION FINE-STRUCTURE - ITS STRENGTHS AND LIMITATIONS AS A STRUCTURAL TOOL. *Rev. Mod. Phys.* **53**, 769-806 (1981).
34. C. Boulesteix, M. Bensalem, B. Yangui, DOMAIN-STRUCTURES AND PLASTICITY OF FERROELASTIC MATERIALS - CASE OF RARE-EARTH SESQUIOXIDES AND YBA2CU3O7. *Journal of the Less-Common Metals* **156**, 29-41 (1989).
35. E. K. H. Salje, Ferroelastic domain walls as templates for multiferroic devices. *Journal of Applied Physics* **128**, 8 (2020).
36. K. Dörr, FERROELASTIC DOMAINS Springy expansion. *Nature Materials* **15**, 497-498 (2016).
37. B. H. Toby, R. B. Von Dreele, GSAS-II: the genesis of a modern open-source all purpose crystallography software package. *Journal of Applied Crystallography* **46**, 544-549 (2013).
38. R. B. Neder, F. Frey, H. Schulz, DIFFRACTION THEORY FOR DIFFUSE-SCATTERING BY CORRELATED MICRODOMAINS IN MATERIALS WITH SEVERAL ATOMS PER UNIT-CELL. *Acta Crystallographica Section A* **46**, 792-798 (1990).
39. K. P. McKenna, F. Hofer, D. Gilks, V. K. Lazarov, C. L. Chen, Z. C. Wang, Y. Ikuhara, Atomic-scale structure and properties of highly stable antiphase boundary defects in Fe3O4. *Nature Communications* **5**, 8 (2014).
40. E. K. H. Salje, APPLICATION OF LANDAU THEORY FOR THE ANALYSIS OF PHASE-TRANSITIONS IN MINERALS. *Phys. Rep.-Rev. Sec. Phys. Lett.* **215**, 49-99 (1992).
41. G. Baldinozzi, D. Simeone, D. Gosset, M. Dutheil, Neutron diffraction study of the size-induced tetragonal to monoclinic phase transition in zirconia nanocrystals. *Physical Review Letters* **90**, 4 (2003).
42. E. C. O'Quinn, K. E. Sickafus, R. C. Ewing, G. Baldinozzi, J. C. Neuefeind, M. G. Tucker, A. F. Fuentes, D. Drey, M. K. Lang, Predicting short-range order and correlated phenomena in disordered crystalline materials. *Sci. Adv.* **6**, 8 (2020).
43. J. Shamblin, M. Feygenson, J. Neuefeind, C. L. Tracy, F. X. Zhang, S. Finkeldei, D. Bosbach, H. D. Zhou, R. C. Ewing, M. Lang, Probing disorder in isometric pyrochlore and related complex oxides. *Nature Materials* **15**, 507-+ (2016).

44. J. Shamblin, C. L. Tracy, R. I. Palomares, E. C. O'Quinn, R. C. Ewing, J. Neuefeind, M. Feygenson, J. Behrens, C. Trautmann, M. Lang, Similar local order in disordered fluorite and aperiodic pyrochlore structures. *Acta Materialia* **144**, 60-67 (2018).
45. E. C. O'Quinn, C. L. Tracy, W. F. Cureton, R. Sachan, J. C. Neuefeind, C. Trautmann, M. K. Lang, Multi-scale investigation of heterogeneous swift heavy ion tracks in stannate pyrochlore. *J. Mater. Chem. A* **9**, 16982-16997 (2021).
46. C. K. Chung, E. C. O'Quinn, J. C. Neuefeind, A. F. Fuentes, H. W. Xu, M. Lang, A. Navrotsky, Thermodynamic and structural evolution of mechanically milled and swift heavy ion irradiated Er2Ti2O7 pyrochlore. *Acta Materialia* **181**, 309-317 (2019).
47. K. E. Sickafus, L. Minervini, R. W. Grimes, J. A. Valdez, M. Ishimaru, F. Li, K. J. McClellan, T. Hartmann, Radiation tolerance of complex oxides. *Science* **289**, 748-751 (2000).
48. P. F. McMillan, New materials from high-pressure experiments. *Nature Materials* **1**, 19-25 (2002).
49. C. Yang, K. Trachenko, S. Hull, I. T. Todorov, M. T. Dove, Emergence of microstructure and oxygen diffusion in yttrium-stabilized cubic zirconia. *Physical Review B* **97**, 9 (2018).
50. M. Fèvre, A. Finel, R. Caudron, Local order and thermal conductivity in yttria-stabilized zirconia.: I.: Microstructural investigations using neutron diffuse scattering and atomic-scale simulations -: art. no. 104117. *Physical Review B* **72**, 13 (2005).
51. K. P. Kelley, A. N. Morozovska, E. A. Eliseev, Y. T. Liu, S. S. Fields, S. T. Jaszewski, T. Mimura, S. Calderon, E. C. Dickey, J. F. Ihlefeld, S. V. Kalinin, Ferroelectricity in hafnia controlled via surface electrochemical state. *Nature Materials*, 10 (2023).
52. S. Petzold, S. U. Sharath, J. Lemke, E. Hildebrandt, C. Trautmann, L. Alff, Heavy Ion Radiation Effects on Hafnium Oxide-Based Resistive Random Access Memory. *IEEE Trans. Nucl. Sci.* **66**, 1715-1718 (2019).
53. M. Lederer, T. Vogel, T. Kämpfe, N. Kaiser, E. Piros, R. Olivo, T. Ali, S. Petzold, D. Lehninger, C. Trautmann, L. Alff, K. Seidel, Heavy ion irradiation induced phase transitions and their impact on the switching behavior of ferroelectric hafnia. *Journal of Applied Physics* **132**, 064102 (2022).
54. A. Parija, G. R. Waetzig, J. L. Andrews, S. Banerjee, Traversing Energy Landscapes Away from Equilibrium: Strategies for Accessing and Utilizing Metastable Phase Space. *J. Phys. Chem. C* **122**, 25709-25728 (2018).
55. R. Thomas, J. F. Scott, D. N. Bose, R. S. Katiyar, Multiferroic thin-film integration onto semiconductor devices. *Journal of Physics-Condensed Matter* **22**, 17 (2010).
56. B. J. Campbell, H. T. Stokes, D. E. Tanner, D. M. Hatch, ISODISPLACE: a web-based tool for exploring structural distortions. *Journal of Applied Crystallography* **39**, 607-614 (2006).
57. A. P. Drozdov, M. I. Eremets, I. A. Troyan, V. Ksenofontov, S. I. Shylin, Conventional superconductivity at 203 kelvin at high pressures in the sulfur hydride system. *Nature* **525**, 73-+ (2015).
58. L. J. Zhang, Y. C. Wang, J. Lv, Y. M. Ma, Materials discovery at high pressures. *Nat. Rev. Mater.* **2**, 16 (2017).
59. H. M. Rietveld, A PROFILE REFINEMENT METHOD FOR NUCLEAR AND MAGNETIC STRUCTURES. *Journal of Applied Crystallography* **2**, 65-& (1969).

60. J. F. Ziegler, M. D. Ziegler, J. P. Biersack, SRIM - The stopping and range of ions in matter (2010). *Nuclear Instruments & Methods in Physics Research Section B-Beam Interactions with Materials and Atoms* **268**, 1818-1823 (2010).
61. R. I. Palomares, J. Shamblin, C. L. Tracy, J. Neuefeind, R. C. Ewing, C. Trautmann, M. Lang, Defect accumulation in swift heavy ion-irradiated CeO2 and ThO2. *J. Mater. Chem. A* **5**, 12193-12201 (2017).
62. X. B. Shi, S. Ghose, E. Dooryhee, Performance calculations of the X-ray powder diffraction beamline at NSLS-II. *J. Synchrot. Radiat.* **20**, 234-242 (2013).
63. J. D. Beal, K. D. Berry, R. A. Riedel, L. L. Funk, W. B. Reynolds, Y. Diawara, The NOMAD instrument neutron detector array at the SNS. *Nucl. Instrum. Methods Phys. Res. Sect. A-Accel. Spectrom. Dect. Assoc. Equip.* **1018**, 9 (2021).
64. C. L. Farrow, P. Juhas, J. W. Liu, D. Bryndin, E. S. Bozin, J. Bloch, T. Proffen, S. J. L. Billinge, PDFfit2 and PDFgui: computer programs for studying nanostructure in crystals. *Journal of Physics-Condensed Matter* **19**, 7 (2007).
65. M. Lang, C. L. Tracy, R. I. Palomares, F. X. Zhang, D. Severin, M. Bender, C. Trautmann, C. Park, V. B. Prakapenka, V. A. Skuratov, R. C. Ewing, Characterization of ion-induced radiation effects in nuclear materials using synchrotron x-ray techniques. *Journal of Materials Research* **30**, 1366-1379 (2015).
66. B. Ravel, M. Newville, ATHENA, ARTEMIS, HEPHAESTUS: data analysis for X-ray absorption spectroscopy using IFEFFIT. *J. Synchrot. Radiat.* **12**, 537-541 (2005).
67. R. Ruh, H. J. Garrett, R. F. Domagala, N. M. Tallan, SYSTEM ZIRCONIA-HAFNIA. *Journal of the American Ceramic Society* **51**, 23-+ (1968).
68. Y. Al-Khatatbeh, K. K. M. Lee, B. Kiefer, Phase relations and hardness trends of ZrO2 phases at high pressure. *Physical Review B* **81**, 10 (2010).
69. B. Schuster, M. Lang, R. Klein, C. Trautmann, R. Neumann, A. Benyagoub, Structural phase transition in ZrO2 induced by swift heavy ion irradiation at high-pressure. *Nuclear Instruments & Methods in Physics Research Section B-Beam Interactions with Materials and Atoms* **267**, 964-968 (2009).
70. E. H. Kisi, C. J. Howard, R. J. Hill, CRYSTAL-STRUCTURE OF ORTHORHOMBIC ZIRCONIA IN PARTIALLY STABILIZED ZIRCONIA. *Journal of the American Ceramic Society* **72**, 1757-1760 (1989).
71. S. E. Reyes-Lillo, K. F. Garrity, K. M. Rabe, Antiferroelectricity in thin-film ZrO2 from first principles. *Physical Review B* **90**, 5 (2014).
72. G. M. Rignanese, F. Detraux, X. Gonze, A. Pasquarello, First-principles study of dynamical and dielectric properties of tetragonal zirconia. *Physical Review B* **64**, 7 (2001).

Acknowledgments

Funding: This work was supported by the U.S. Department of Energy, Office of Science, Basic Energy Sciences, under Award DE-SC0024140. A.P.S. acknowledges support from the University Nuclear Leadership Program through an NEUP Fellowship. The research at ORNL's Spallation Neutron Source was sponsored by the Scientific User Facilities Division, Office of Basic Energy Sciences, U.S. DOE. This research also used the X-ray powder diffraction beamline of the National Synchrotron Light Source II, a U.S. DOE

Office of Science User Facility operated for the DOE Office of Science by Brookhaven National Laboratory under contract no. DE-SC0012704. The results presented here are based on a UMAT experiment, which was performed at the X0-beamline of the UNILAC at the GSI Helmholtzzentrum fuer Schwerionenforschung, Darmstadt (Germany) in the frame of FAIR Phase-0.

Author contributions: A.P.S. and M.K.L. conceived and designed the study. I.G. and G.B. synthesized the nanocrystalline sample. A.P.S. prepared samples for ion irradiation and characterization by X-ray and neutron scattering techniques. C.T. managed the ion irradiation experiments. J.N. aided with neutron scattering measurements and data reduction. J.L. and X.G. analyzed the EXAFS data. A.P.S. and E.C.O. performed the Rietveld and small-box refinements. A.P.S. and G.B. constructed and refined the supercell model. A.P.S., E.C.O., M.K.L., and R.C.E. wrote the manuscript with input from all authors.

Competing interests: Authors declare that they have no competing interests.

Data and materials availability: All data needed to evaluate the conclusions in the paper are present in the paper and/or the Supplementary Materials.

Figures and Tables

Fig. 1. XRD patterns and neutron PDFs for microcrystalline (bulk), irradiated, and nanocrystalline ZrO_2. (**A**) X-ray diffraction (XRD) patterns for each sample. Miller indices denote prominent diffraction peaks, and asterisks indicate peaks from a secondary phase (< 5% phase fraction). (**B**) Neutron pair distribution functions (PDFs) for each sample. Open circles denote the measured PDFs, red curves represent fits of the monoclinic (bulk) or tetragonal (nano and irradiated) model, and magenta curves show the difference between the data and the fit. All data sets are offset vertically for ease of visualization.

Fig. 2. Qualitative energy landscape of the two-step phase transformation pathway between the tetragonal ($P4_2/nmc$) and monoclinic ($P2_1/c$) phases. This transformation involves a saddle point of the Landau free energy: an unstable orthorhombic (*Pbcn*) intermediate polymorph. The transformation pathway is described by the amplitudes of the two phonons M1 and M3 for (**A**) an ideal crystal and for (**B**) a defective crystalline structure, alongside (**C**) the structure of each phase with Zr and O atoms shown in green and red, respectively. Temperature is analogous to free energy in this representation.

Fig. 3. PDF and EXAFS data describe short-range order (SRO). (**A**) Neutron PDF reveals that the short-range order of nanocrystalline ZrO_2 is best fit using an orthorhombic *Pbcn* phase, which is independently confirmed by (**B**) the Fourier transform of Extended X-ray Absorption Fine-Structure (EXAFS) spectra of the same sample. Magenta curves show the difference between the models (colored lines) and the data (black circles), and weighted residuals are reported as R_w.

Fig. 4. Orientational relation between derivative orthorhombic variants and the tetragonal phase. Orthorhombic, Pbcn unit cells (solid blue borders) have twice the volume of the tetragonal, $P4_2/nmc$ unit cell (dashed black borders). Zr cations are shown in green; oxygen anions are shown in red. Arrows indicate the direction of the static displacement from the ideal tetragonal site.

Fig. 5. Supercell model with simulated XRD and PDF. (**A**) A supercell composed of four orthorhombic domains, differentiated by the direction and phase of the displacements corresponding to the M1 phonon, produces an average, long-range structure that is tetragonal, as demonstrated by (**B**) the simulated XRD pattern of the supercell overlaid with tetragonal peak indices and the measured diffraction pattern of nano-ZrO_2. (**C**) Simulated PDF describes the transition between orthorhombic SRO (orange) and tetragonal LRO (blue).

Fig. 6. Metastable phase synthesis routes. Various synthesis pathways produce metastable phases in which statically distorted structural units, distinct from the equilibrium phase at room temperature, form apparent crystalline structures that are not representative of any physical atomic configuration within the material. The SRO orthorhombic structures of tetragonal HfO_2(*) and cubic ZrO_2(**) are different than the orthorhombic (*Pbcn*) phase of tetragonal zirconia.

Figures and Tables

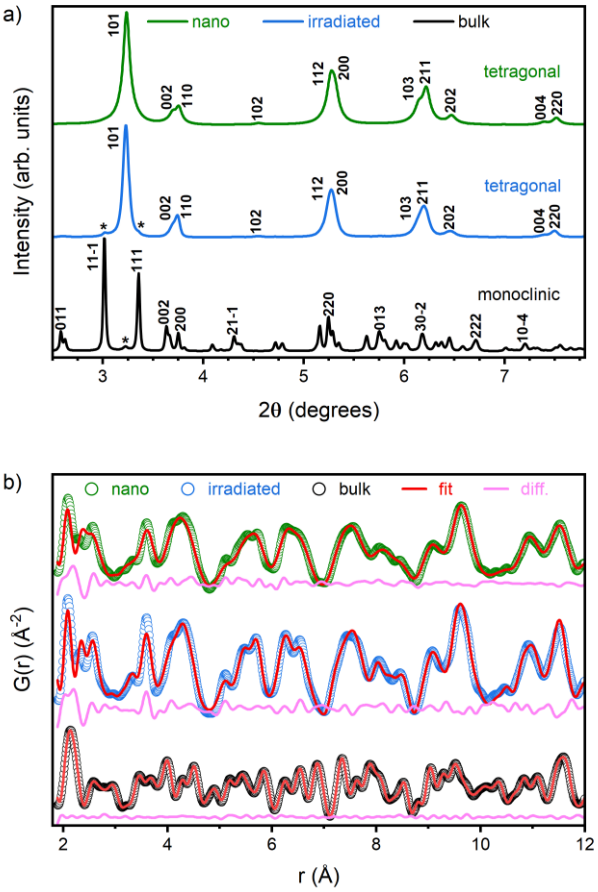

Fig. 1. XRD patterns and neutron PDFs for microcrystalline (bulk), irradiated, and nanocrystalline ZrO_2. (**A**) X-ray diffraction (XRD) patterns for each sample. Miller indices denote prominent diffraction peaks, and asterisks indicate peaks from a secondary phase (< 5% phase fraction). (**B**) Neutron pair distribution functions (PDFs) for each sample. Open circles denote the measured PDFs, red curves represent fits of the monoclinic (bulk) or tetragonal (nano and irradiated) model, and magenta curves show the difference between the data and the fit. All data sets are offset vertically for ease of visualization.

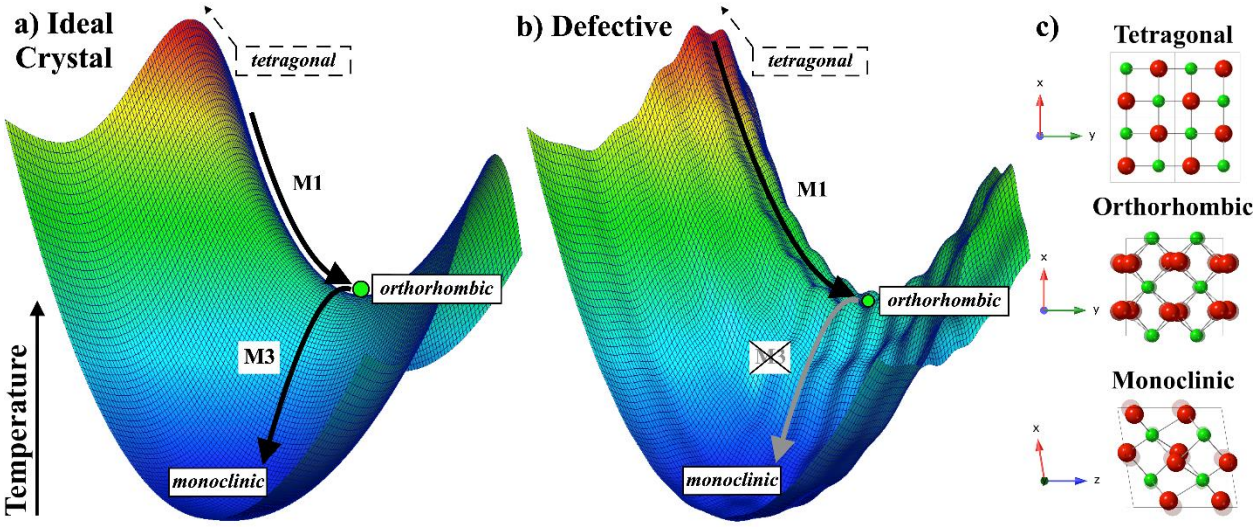

Fig. 2. Qualitative energy landscape of the two-step phase transformation pathway between the tetragonal (*$P4_2/nmc$*) and monoclinic (*$P2_1/c$*) phases. This transformation involves a saddle point of the Landau free energy: an unstable orthorhombic (*Pbcn*) intermediate polymorph. The transformation pathway is described by the amplitudes of the two phonons M1 and M3 for (**A**) an ideal crystal and for (**B**) a defective crystalline structure, alongside (**C**) the structure of each phase with Zr and O atoms shown in green and red, respectively. Temperature is analogous to free energy in this representation.

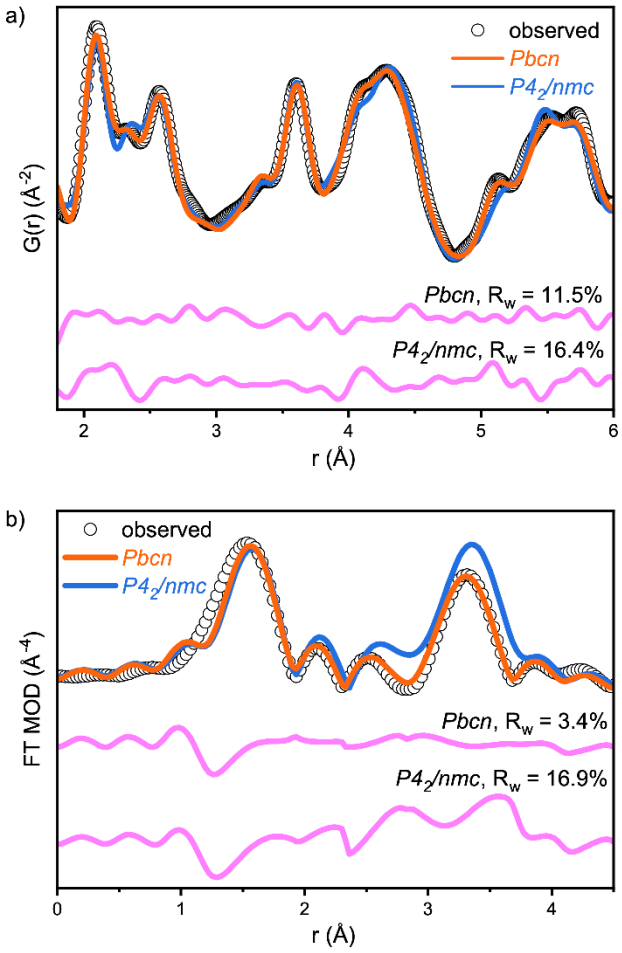

Fig. 3. PDF and EXAFS data describe short-range order (SRO). (**A**) Neutron PDF reveals that the short-range order of nanocrystalline ZrO_2 is best fit using an orthorhombic *Pbcn* phase, which is independently confirmed by (**B**) the Fourier transform of Extended X-ray Absorption Fine-Structure (EXAFS) spectra of the same sample. Magenta curves show the difference between the models (colored lines) and the data (black circles), and weighted residuals are reported as R_w.

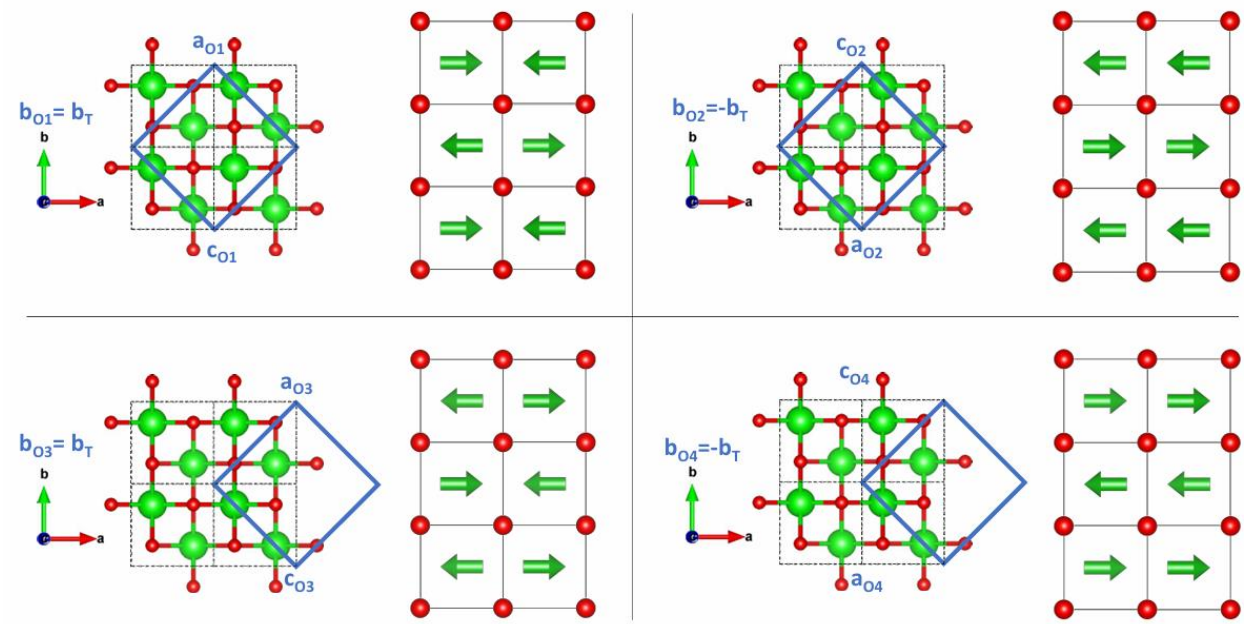

Fig. 4. Orientational relation between derivative orthorhombic variants and the tetragonal phase. Orthorhombic, Pbcn unit cells (solid blue borders) have twice the volume of the tetragonal, $P4_2/nmc$ unit cell (dashed black borders). Zr cations are shown in green; oxygen anions are shown in red. Arrows indicate the direction of the static displacement from the ideal tetragonal site.

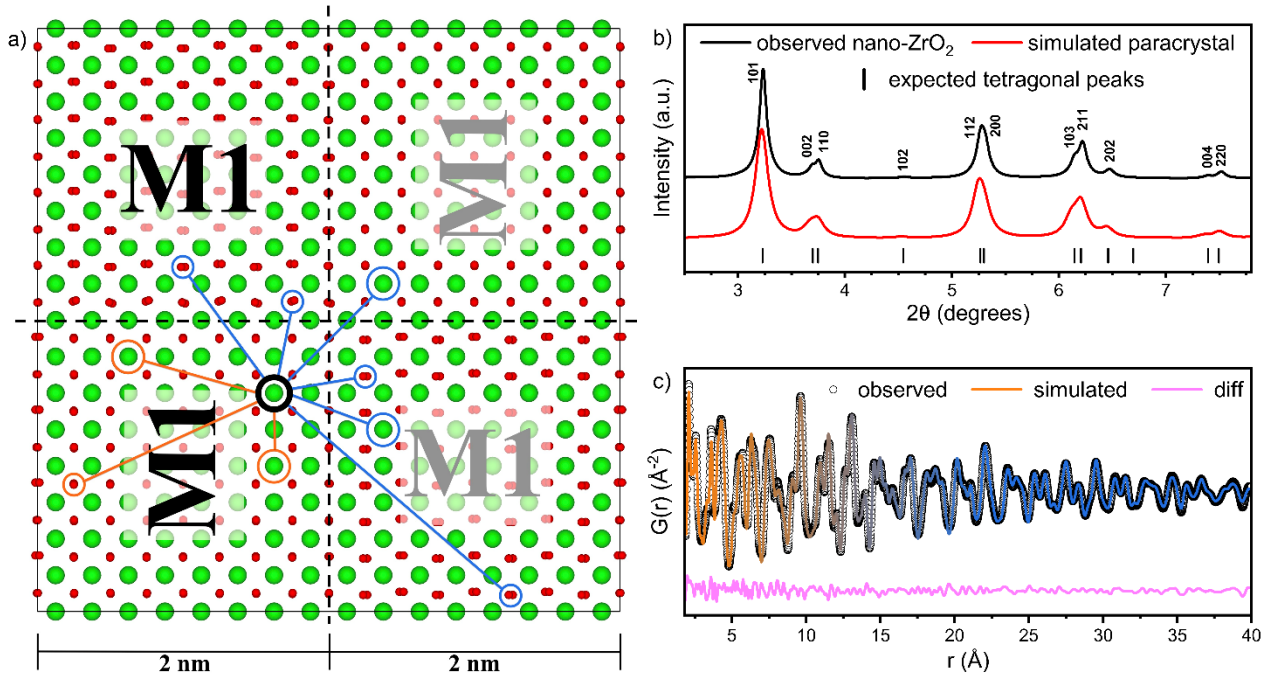

Fig. 5. Supercell model with simulated XRD and PDF. (**A**) A supercell composed of four orthorhombic domains, differentiated by the direction and phase of the displacements corresponding to the M1 phonon, produces an average, long-range structure that is tetragonal, as demonstrated by (**B**) the simulated XRD pattern of the supercell overlaid with tetragonal peak indices and the measured diffraction pattern of nano-ZrO_2. (**C**) Simulated PDF describes the transition between orthorhombic SRO (orange) and tetragonal LRO (blue).

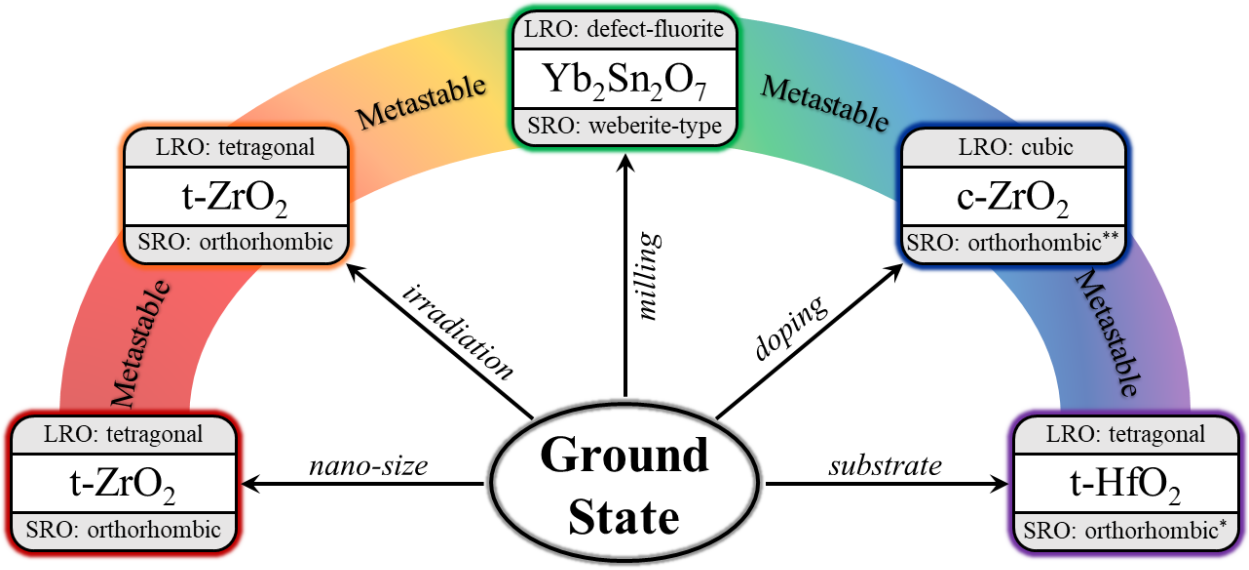

Fig. 6. Metastable phase synthesis routes. Various synthesis pathways produce metastable phases in which statically distorted structural units, distinct from the equilibrium phase at room temperature, form apparent crystalline structures that are not representative of any physical atomic configuration within the material. The SRO orthorhombic structures of tetragonal HfO_2(*) and cubic ZrO_2(**) are different than the orthorhombic (*Pbcn*) phase of tetragonal zirconia.

Science Advances
AAAS

Supplementary Materials for

Atomic-Scale Structure of ZrO_2: Formation of Metastable Polymorphs

Alexandre P. Solomon *et al.*

*Corresponding author. Email: mlang2@utk.edu

This file includes:

Supplementary Text
Figs. S1 to S6
Tables S1 to S2

Supplementary Text

Polymorphism in ZrO_2

ZrO_2 is a binary oxide with an atomic structure related to that of fluorite. At standard conditions, bulk ZrO_2 crystals form the monoclinic (m) phase with space group $P2_1/c$ (Fig. S1). At approximately 1400 K, the m-phase transitions to the tetragonal (t) $P4_2/nmc$ phase. Then, at approximately 2600 K the t-phase transitions to the cubic (c) $Fm\text{-}3m$ phase (*18, 67*). Furthermore, near ambient temperatures, the m-phase of ZrO_2 transitions to the high-pressure orthorhombic (hp-o; orthorhombic I) *Pbca* phase at approximately 4 to 10 GPa (*68, 69*). All these phases have a center of symmetry and are not polar, thus they do not possess the remnant polarization. The ferroelectricity in ZrO_2 originates from the polar orthorhombic (ferro-o) $Pca2_1$ phase (*20*). This crystal phase was already reported in 1989 (*70*), though the electric characterization was not performed then, so that the ferroelectric properties were not unveiled until 2011. There are also other crystal phases, including polar phases, which were theoretically predicted (*71*). However, these phases have higher energy in comparison to the low energy m, hp-o, ferro-o, and t-phases.

Neutron scattering data and refinements

Spallation neutron diffraction (Fig. S2) supplemented synchrotron X-ray diffraction experiments, and Rietveld analysis of the neutron diffraction patterns (Fig. S3) similarly indicated tetragonal long-range order in both metastable ZrO_2 samples. Pair distribution function (PDF) analysis of neutron total scattering data (Fig. S4) revealed that the short-range order is distinct from any known equilibrium structure and is best described by the *Pbcn* model.

Figure S5 displays results of a set of preliminary refinements that use a model consisting of an uncorrelated mixture of two phases of tetragonal and orthorhombic symmetry, respectively. In these refinements, the contributions of the two phases are additive, corresponding to a spatially non-uniform uncorrelated binary mixture. The boxcar refinement was performed analyzing a moving *r*-interval of fixed length. It shows that the PDF signal in the interval is exclusively orthorhombic at short *r*-values, and it becomes exclusively tetragonal above $r = 20$ Å. Obviously, this result is incompatible with any true physical picture of an uncorrelated binary phase mixture. On the other hand, it clearly supports the image of a collection of nanocrystals made of an assembly of orthorhombic ferroelastic domains. The model also provides a good estimate of the characteristic correlation length of the individual orthorhombic domains ($r = 20$ Å). This value was used to choose a reasonable size of the domains of orthorhombic symmetry and to assemble them in a supercell consisting of all possible ferroelastic orthorhombic variants. This system, built using the broken symmetry elements of the tetragonal long-range symmetry, provides the correct long-range ensemble average that restores the broken tetragonal symmetry at large *r*-values.

Displacive transformation driven by temperature

The high-temperature polymorph of zirconia is cubic. Lowering temperature below 1300 – 1400 K at ambient pressure produces a tetragonal polymorph. This phase change is usually described by a displacive mechanism involving the zone boundary phonon belonging to the irreducible representation X_2^- (*72*). This structure is non-polar, described by the space group symmetry

P4₂/nmc, and it is characterized by antiparallel shifts of the O atoms along the tetragonal axis direction. The tetragonal lattice is not collinear with the cubic lattice, and the tetragonal orientation is defined by the following lattice transformation of the cubic lattice:

$$[a_T \quad b_T \quad c_T] = [a_C \quad b_C \quad c_C]\begin{bmatrix} 1/2 & -1/2 & 0 \\ 1/2 & 1/2 & 0 \\ 0 & 0 & 1 \end{bmatrix}.$$

Further lowering the temperature leads to another phase transformation to a monoclinic polymorph. The mechanism of this phase transition was described by Negita (*32*), and it involves the softening of a zone boundary phonon belonging to the M1 irreducible representation of the tetragonal structure, followed immediately by another phonon belonging to the M3 irreducible representation (alternatively, this can be described by a zone center irreducible representation Γ^+_3 in the lattice produced by the condensation of M1). The unstable nature of this phase has been described in terms of an energy landscape with a saddle point shape (coordinates are the amplitudes of the M1 and M3 phonons). A pre-transitional signature of these displacive instabilities was obtained by Rietveld refinement of neutron powder diffraction data of the high-temperature tetragonal polymorph (*19*). The intermediate unstable phase obtained after the M1 phonon instability has symmetry *Pbcn*, and the relation of this orthorhombic lattice relative to the tetragonal lattice is described by the following transformation matrix followed by a $\mathbf{b}_O/2$ origin shift:

$$[a_O \quad b_O \quad c_O] = [a_T \quad b_T \quad c_T]\begin{bmatrix} -1 & 0 & 1 \\ 1 & 0 & 1 \\ 0 & 1 & 0 \end{bmatrix}.$$

Therefore, the former four-fold axis $\mathbf{c}_T$ now aligns along $\mathbf{b}_O$. The M1 phonon branch, which couples with strain tensor components of symmetry Γ^+_4, leads to the differentiation of the orthorhombic a and c axes, affecting the final Zr–O bond lengths. Using a frozen-phonon picture for the phonon branch belonging to this M1 irreducible representation, the structural parameters describing the low-temperature orthorhombic variants can be organized as a superposition of polarization vectors containing the cartesian components of the displacements of each one of the independent atoms. This orthorhombic daughter phase is then a complex medium-range order (MRO) assembly consisting of four *Pbcn* ferroelastic variants (Fig. 4), providing the mathematical background for the model construction. Each variant is described by a unique combination of symmetry operations, a different superlattice basis, and a specific origin choice.

In bulk samples, the intermediate orthorhombic symmetry is immediately broken by the sudden condensation of the M3 phonon branch that also couples with a shear strain component of symmetry Γ_5^+, ultimately producing the monoclinic ground state. This instability of symmetry M3 in the tetragonal lattice description, or equivalently Γ^+_3 in the orthorhombic lattice description, brings the system to the monoclinic phase of symmetry $P2_1/c$ (either M3, or equivalently Γ^+_3). This changes the lattice again, aligning the $\mathbf{c}_M$ direction along the former four-fold axis of the tetragonal phase:

$$[a_M \quad b_M \quad c_M] = [a_O \quad b_O \quad c_O]\begin{bmatrix} 0 & 1 & 0 \\ 0 & 0 & 1 \\ 1 & 0 & 0 \end{bmatrix}.$$

Detailed structural parameters of orthorhombic ZrO_2

Neutron PDF fitting parameters of both metastable samples of ZrO_2 (nanocrystalline and ion-irradiated) are provided in Table S1.

EXAFS fitting parameters of metastable, nanocrystalline ZrO_2 are provided in Table S2. Reported uncertainties were output from the structural refinements. Coordination numbers (CNs) were fixed during the fitting. The minimum Debye-Waller factor was limited to 1.0×10^3 Å^2. The S02 was set to 1.0 for both fittings.

Metastable Pyrochlore

$Yb_2Sn_2O_7$ pyrochlore was ball-milled for 33 hours, and the transformation to the metastable, defect fluorite phase was observed by X-ray and neutron diffraction using the same procedure as for ZrO_2. A neutron total scattering experiment was performed to probe the SRO of the metastable phase, and the PDF is shown in Figure S6. Neither the pyrochlore (ground-state) nor the defect fluorite (metastable) phase could reproduce the experimental PDF. Rather, the atomic-scale structure of the metastable phase was best described using an orthorhombic, weberite-type (*Ccmm*) structural model.

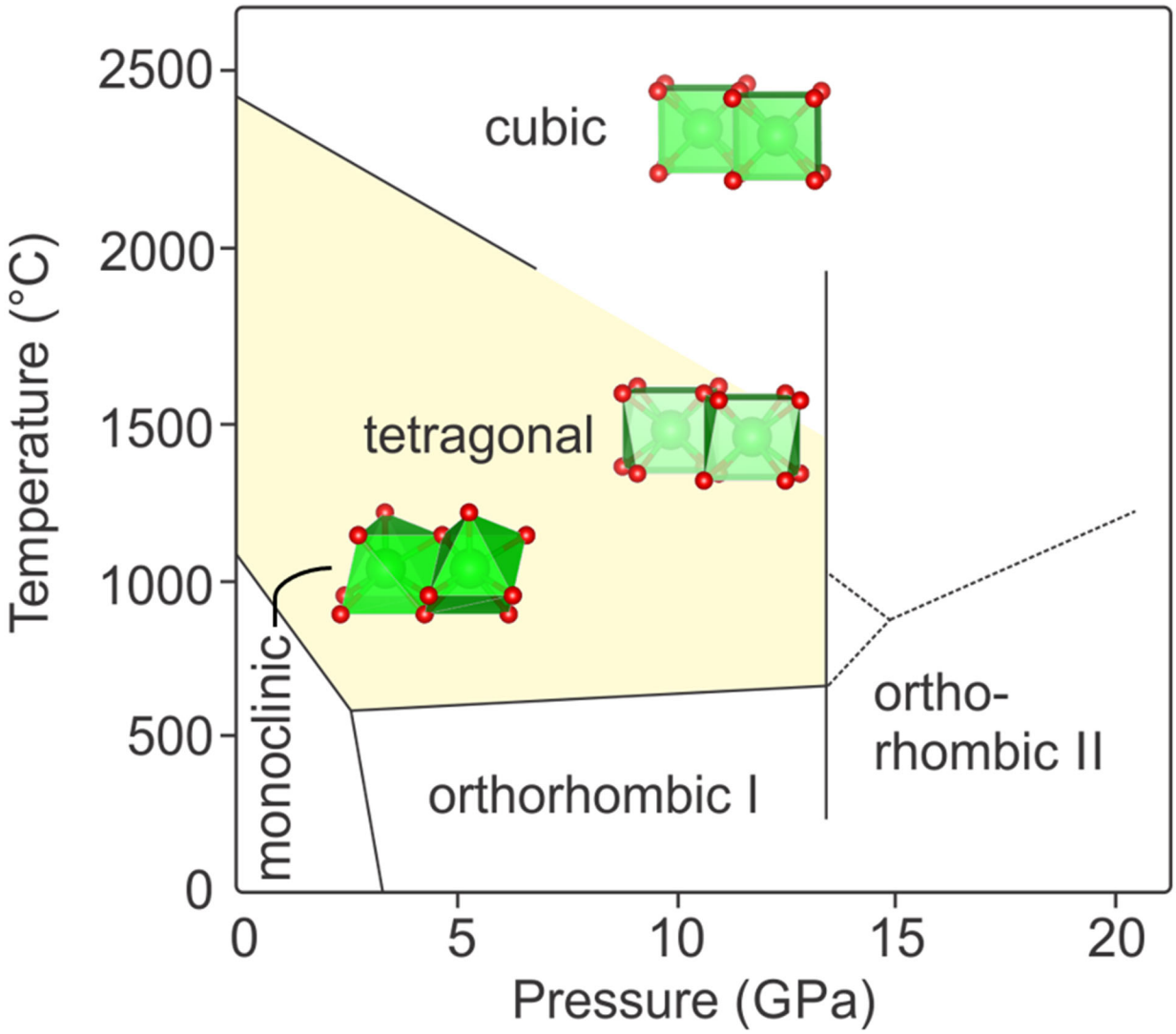

Fig. S1. Phase diagram of ZrO_2 (*69*). The equilibrium structures accessible at different temperatures are shown with Zr cations in green and oxygen anions in red.

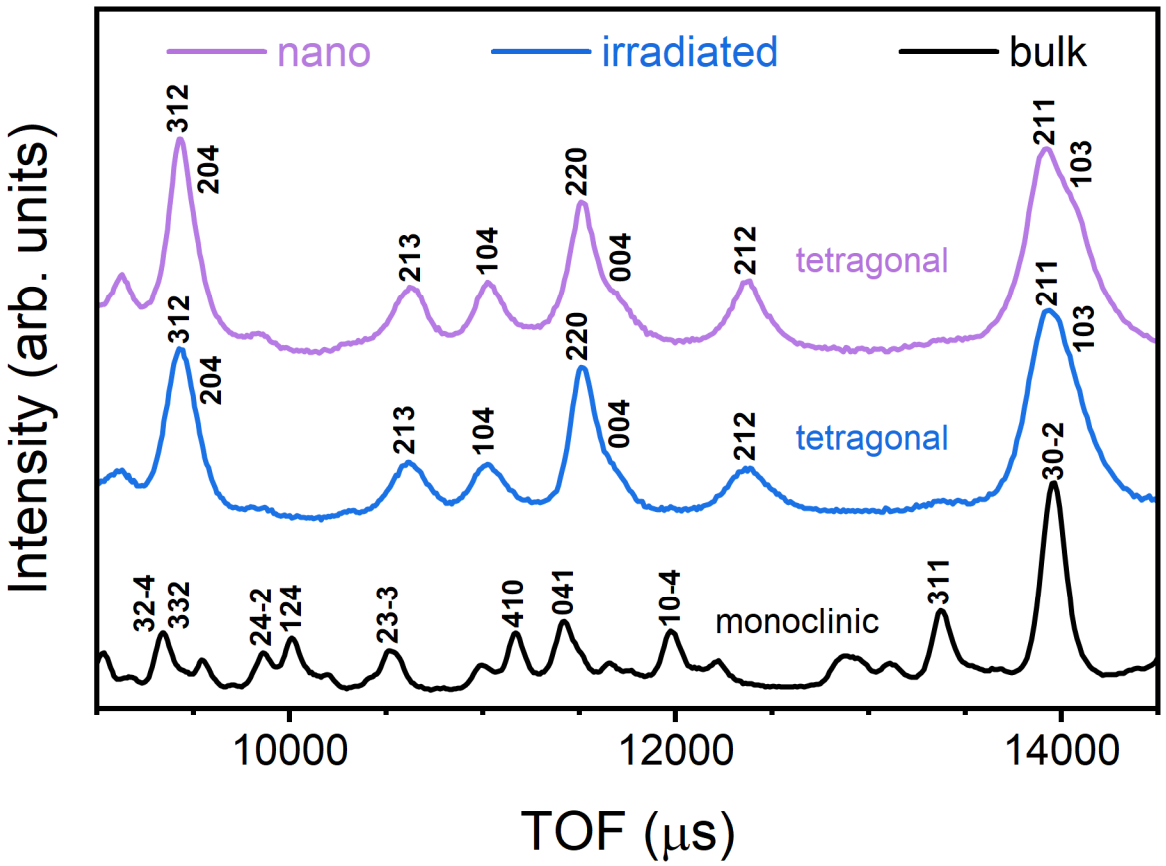

Fig. S2. Neutron diffraction patterns (NOMAD bank 4) shown for bulk, irradiated (1.47 GeV Au, 10^{13} ions cm^{-2}), and nanocrystalline ZrO_2. Miller indices denote prominent diffraction peaks. All peaks are indexed by the monoclinic and tetragonal phases. The diffraction patterns are offset vertically for ease of visualization.

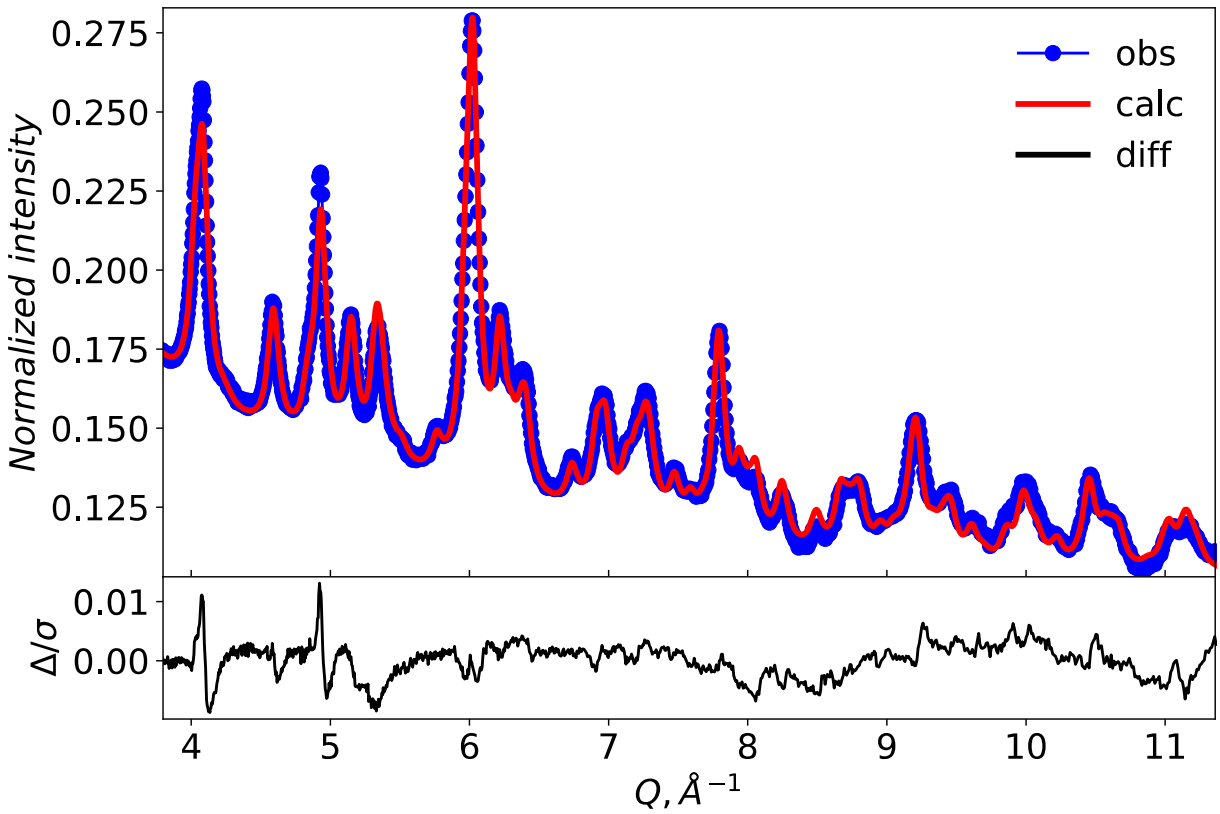

Fig. S3. Representative Rietveld refinement of neutron diffraction pattern for nanocrystalline ZrO_2. The refinement was performed using the high temperature tetragonal phase polymorph and data collected using bank 4 of the NOMAD instrument. Blue circles represent experimental data, the red curve was calculated from the refined structure, and the difference curve is given in black.

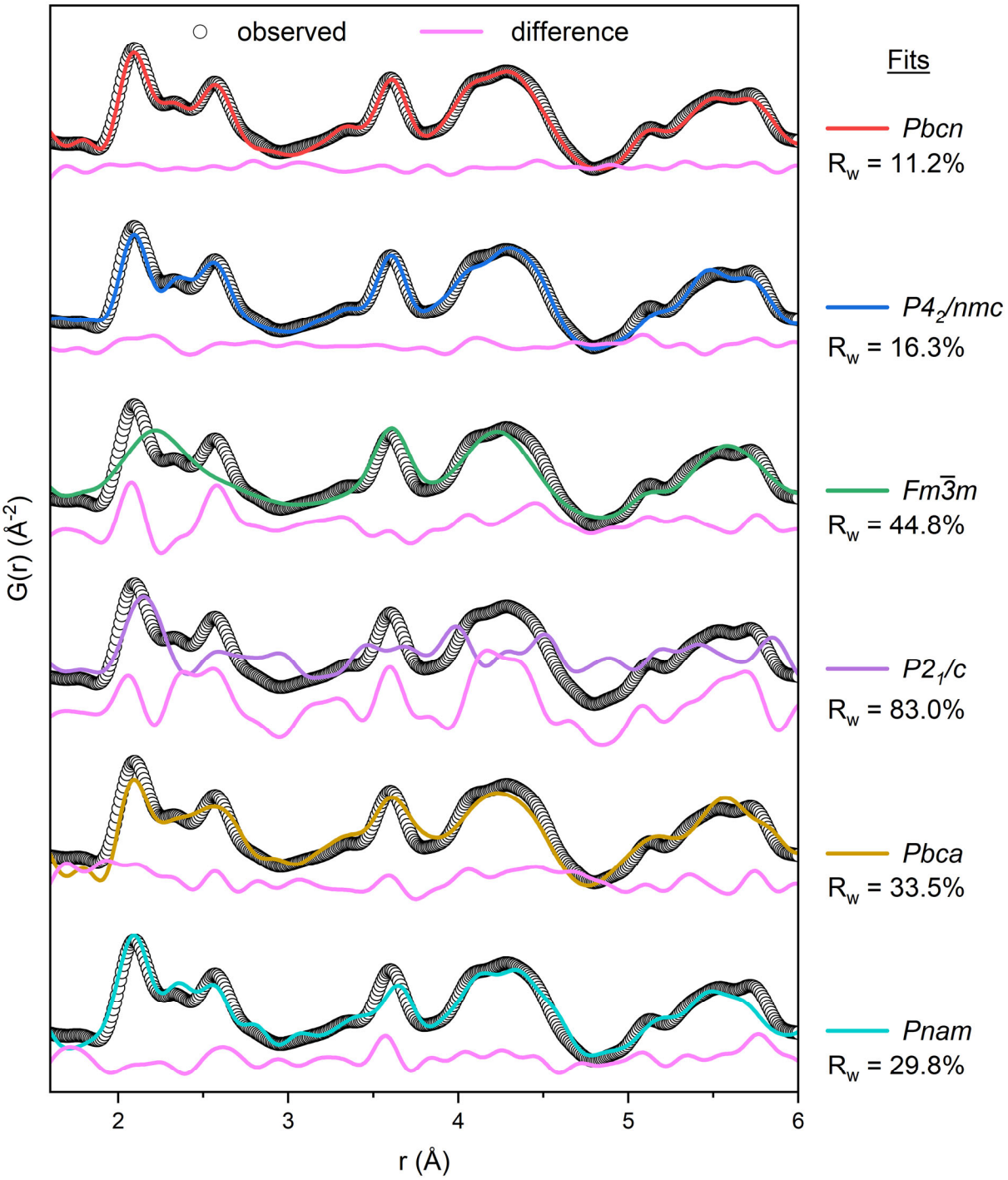

Fig. S4. Fits of known structures to experimental PDF. Calculated fits (colored lines) from small-box refinements of known ZrO_2 structures refined over $1.6 \leq r \leq 6.0$ Å are compared to the experimental PDF (open black circles) of nanocrystalline ZrO_2. The absolutely scaled PDFs are each offset by a constant amount along the y-axis. Respective difference curves are shown in magenta, and weighted residuals are reported as R_w.

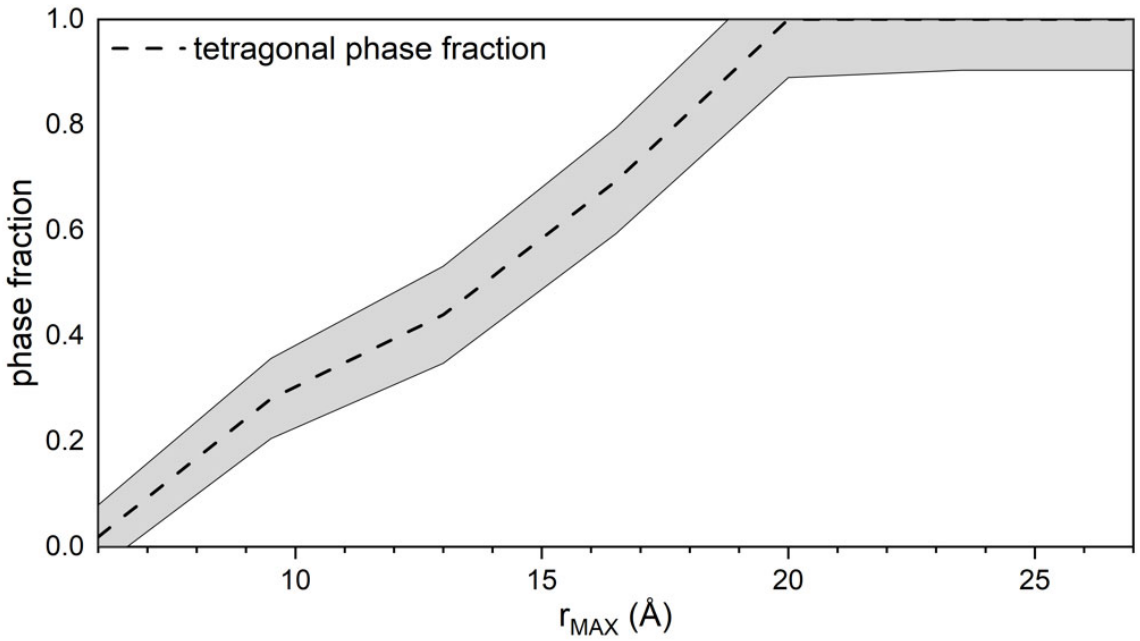

Fig. S5. Phase fractions determined from two-phase boxcar refinements of the nanocrystalline ZrO_2 neutron PDF. Tetragonal and orthorhombic phase fractions exhibit a dependence on the real space range sampled. No tetragonal pair correlations are observed at r-values below ~6–7 Å, and little to no intensity from orthorhombic pair correlations is observed above ~20 Å. Each boxcar spans 4.2 Å (e.g., $1.8 \leq r \leq 6.0$ Å). Phase fractions shown are the mass fractions calculated by PDFgui.

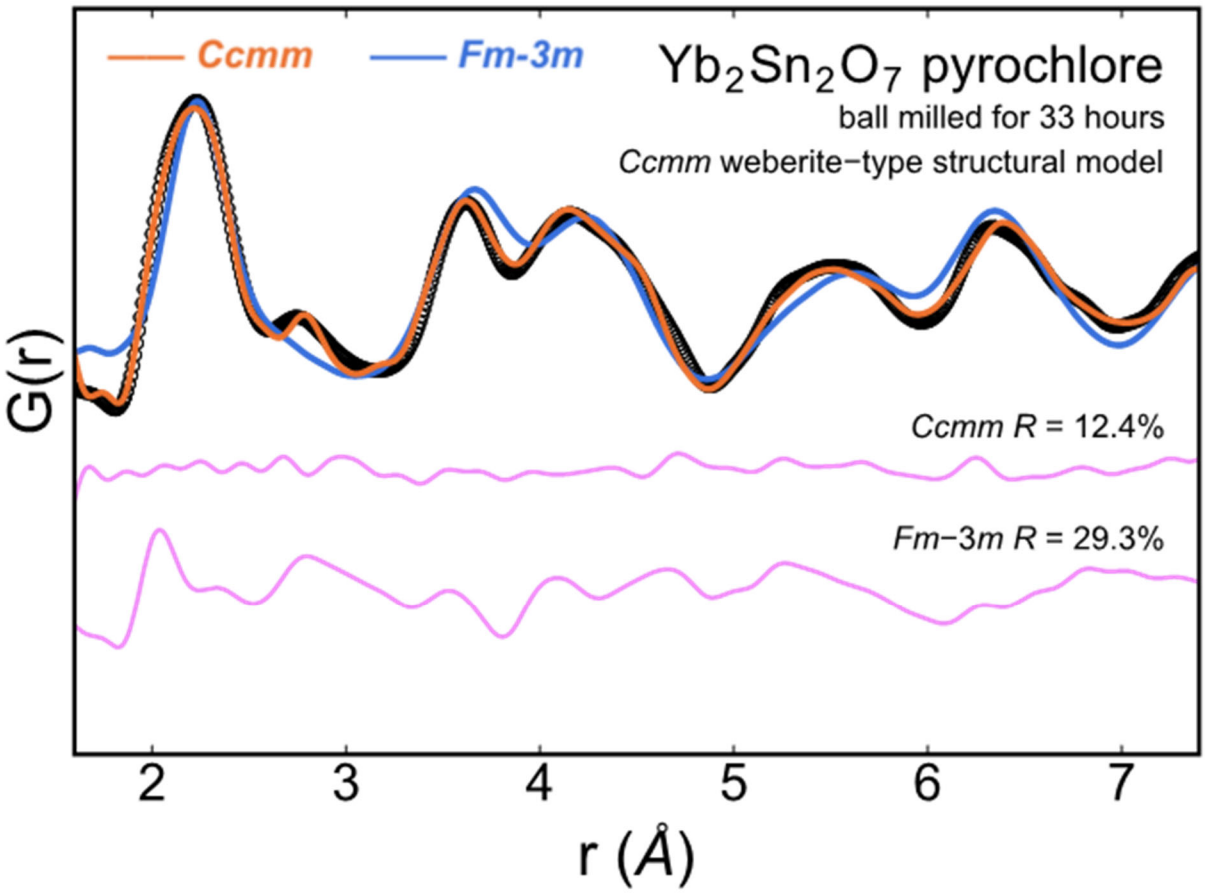

Fig. S6. Neutron pair distribution function of mechanically milled $Yb_2Sn_2O_7$. Fits to the cubic, defect fluorite (Fm-3m) and orthorhombic, weberite-type (*Ccmm*) models are shown in orange and blue, respectively. Magenta curves show the difference between the data (black circles) and the models (colored lines), and weighted residuals are reported as R.

	x	y	*z*	U_{iso} (Å^2)	a (Å)	b (Å)	c (Å)
Nanocrystalline							
Zr1	0	0.744(4)	0.25	0.005(1)	5.04(2)	5.18(2)	5.13(2)
O1	0.733(4)	0.045(2)	0.988(3)	0.012(5)			
Irradiated							
Zr1	0	0.742(3)	0.25	0.005(1)	5.05(2)	5.18(2)	5.13(2)
O1	0.734(4)	0.045(2)	0.988(2)	0.013(5)			

Table S1. Neutron PDF fitting parameters of metastable ZrO_2 samples with *Pbcn* structure. Uncertainties shown represent one standard deviation.

Pbcn					
Path	CN	R (Å)	Sigma ($\times 10^4$ Å^2)	ΔE (eV)	Theor. R (Å)
Zr-O1a	2.0	2.09(1)	10(1)		2.06
Zr-O1b	2.0	2.09(1)	10(1)		2.13
Zr-O1c	2.0	2.20(1)	10(7)		2.27
Zr-O1d	2.0	2.29(1)	10(8)		2.45
Zr-O1-O1a	4.0	3.35(37)	10(1)		3.39
Zr-O1-O1b*	4.0	3.48	10.		3.46
Zr-O1-O1c*	4.0	3.51	10.	-4.0(5)	3.50
Z-O1-O1d*	4.0	3.53	10.		3.56
Zr-Zr1a	2.0	3.58(1)	29(6)		3.58
Zr-Zr1b	4.0	3.69(1)	21(2)		3.60
Zr-Zr1c	4.0	3.50(1)	64(6)		3.63
Zr-Zr1d	2.0	3.61(1)	32(6)		3.71
Zr-O2a	2.0	4.32(8)	10(30)		4.07
Zr-O2b	2.0	4.24(5)	11(60)		4.08
$P4_2/nmc$					
Zr-O1a	4.0	2.10(1)	10(6)		2.09
Zr-O1b	4.0	2.28(1)	46(12)		2.36
Zr-Zr1a	4.0	3.52(1)	13(29)	2.9(7)	3.60
Zr-Zr1b	4.0	3.71(1)	14(3)		3.63
Zr-Zr1c	4.0	3.62(1)	10(3)		3.64

*Fixed parameters

Table S2. EXAFS fitting parameters of nanocrystalline ZrO_2 sample with *Pbcn* and *$P4_2/nmc$* structures.